

Near-Ultraviolet Spectra of Flares on YZ CMi

Suzanne L. Hawley¹, Lucianne M. Walkowicz¹, Joel C. Allred², Jeff A. Valenti³

ABSTRACT

Near-ultraviolet spectroscopic data obtained with the HST STIS instrument on the dMe flare star YZ Canis Minoris (YZ CMi) were analyzed. Flare and quiet intervals were identified from the broadband near-UV light curve, and the spectrum of each flare was separately extracted. Mg II and Fe II line profiles show similar behavior during the flares. Two large flares allowed time-resolved spectra to be analyzed, revealing a very broad component to the Mg II k line profile in at least one flare spectrum (F9b). If interpreted as a velocity, this component requires chromospheric material to be moving with FWHM ~ 250 km sec⁻¹, implying kinetic energy far in excess of the radiative energy. The Mg II k flare line profiles were compared to recent radiative hydrodynamic models of flare atmospheres undergoing electron beam heating. The models successfully predict red enhancements in the line profile with typical velocity of a few km sec⁻¹, but do not reproduce the flares showing blue enhancements, or the strongly broadened line observed in flare F9b. A more complete calculation of redistribution into the line wings, including the effect of collisions with the electron beam, may resolve the origin of the excess line broadening.

Subject headings: stars: low mass — stars: magnetic activity — stars: emission lines — stars: flares — stars: individual (YZ CMi)

1. Introduction

Spectroscopic signatures of flares on M dwarfs have been sporadically explored, mostly at optical wavelengths, since the pioneering observations of UV Ceti by Joy & Humason (1949). Principal features observed during flares include strong continuum radiation rising toward the blue and near-ultraviolet; broad, enhanced hydrogen Balmer series emission lines;

¹Astronomy Department, University of Washington, Box 351580, Seattle, WA 98195

²Physics Department, Drexel University, 3141 Chestnut Street, Philadelphia, PA 19104

³Space Telescope Science Institute, 3700 San Martin Drive, Baltimore, MD 21218

enhanced emission in high temperature lines such as He I, He II, C IV, N V, Si IV; enhanced X-ray emission; and bursts of radio emission (e.g. Kunkel 1967, Jackson et al. 1989, Hawley & Pettersen 1991, Eason et al. 1992, Osten et al. 2005).

YZ Canis Minoris (YZ CMi, also known as Gliese 285), an active dM4.5e star with $V=11.1$ and $d=6\text{pc}$ (Perryman et al. 1997), has been a popular target for flare monitoring campaigns, due to its proximity and strong activity, which improves the chances of observing a flare. Extensive multiwavelength spectroscopic flare studies of YZ CMi include those of Kahler et al. (1982), Worden et al. (1984), and van den Oord et al. (1996).

Previously, no M dwarf flare star has been systematically observed with high-resolution near-ultraviolet spectroscopy in the region where the important chromospheric Mg II h and k lines, and numerous Fe II emission lines, are produced. IUE did not have the sensitivity to provide much time or spectral resolution during flares, although strong Mg II emission was observed from the dM3e star AD Leo during the decay phase of an exceptionally large flare (Hawley & Pettersen 1991). Linsky et al. (1982) carried out an early pioneering study of ultraviolet emission in active cool stars with IUE, while a later comparative study of Mg II h and k emission with X-ray emission was undertaken for a sample of M dwarfs, including YZ CMi, by Mathioudakis & Doyle (1989). Broadband near-ultraviolet emission during flares has been recently studied, using XMM-Newton data by Mitra-Kraev et al. (2005), and using GALEX data by Robinson et al. (2005).

The data presented here were obtained as part of a larger multiwavelength campaign to observe YZ CMi in 2000. We use these near-ultraviolet spectra to examine the Mg II and Fe II emission line profiles in YZ CMi during quiescence and flares, and to study the behavior of the Mg II emission in the flares that are large enough to be subdivided into separate, time-resolved flare spectra. We also compare the observational data for these chromospheric lines with predictions from our new generation of radiative hydrodynamic models (Allred et al. 2005, 2006). The new models incorporate detailed radiative transfer in atmospheres heated by non-thermal electrons and undergoing significant mass motions as heated material flows upward (evaporation) and downward (condensation) within a magnetic loop. The models were designed to predict velocities and line profiles of chromospheric emission lines, and are therefore suitable for comparison with the Mg II observations described here.

2. Observations

The Hubble Space Telescope (HST) observed YZ CMi on 2000 February 5-6, as part of GO program 8129 (PI: R. Robinson). We reanalyze these archival data as part of AR

program 10312 (PI: S. Hawley). The Space Telescope Imaging Spectrograph (STIS, Kimball et al. 1998), was used with the medium resolution NUV echelle grating (E230M) and the 0.2x0.2 arcsec aperture. The E230M spectra have a nearly constant ($\pm 1.5\%$) dispersion of 4.88 km/s per pixel. The line spread function (LSF) for the 0.2x0.2 arcsec aperture has a FWHM of 1.8-1.9 pixels over the wavelength range 2400-2800Å, corresponding to a resolving power of $R=33,000$. These are the only STIS spectra of an M dwarf flare star at NUV wavelengths that exist in the HST archive. Data were obtained during six consecutive orbits, with exposure times ranging from 32 to 40 minutes, over a 6.5 hour total timespan. The MAMA detector timetag mode was used for the observations, resulting in an event list for each exposure that contains the detection time and location of every detected photon.

To construct light curves of the integrated light obtained during each exposure, we used an extraction window that was 11 pixels wide, centered on each echelle order, to assign all timetag events to either source or background regions on the MAMA detector. We then divided each exposure into 100 uniform time bins (19-24 s in duration depending on the individual exposure lengths which range from 32-40 min, see Table 1), obtaining separate light curves for the source and background regions. For each exposure, we fitted the background light curve with a sixth order polynomial, scaled the result by the ratio of source to background pixels, and then subtracted this predicted background from the source light curve to obtain a total observed stellar count rate for each time bin. Errors for each time bin include Poisson noise from the subtracted background.

Figure 1 illustrates the resulting light curves for the six exposures. The flaring and quiet intervals F1-10 and Q1-8 were assigned by qualitative inspection of the light curves, and are labeled on the figure. Table 1 provides relevant information about each spectral interval. Column 1 lists the number of the exposure containing the time interval. Exposure number N maps to HST dataset o59k010N0. The second and third columns give the start and end time of each interval, expressed in minutes since the beginning of each exposure. Column 4 gives the label assigned to each time interval, with Q labels indicating quiet intervals and F labels indicating flare intervals. The numbers were assigned sequentially in time for individual intervals. Columns 5 and 6 give the total count rate and standard deviation for each interval. Although the flaring and quiet intervals were assigned qualitatively, it is clear from these data that the flaring intervals have both higher count rates and larger scatter. The exceptions are the late decay phases of the two large flares, labeled as F2c and F9c. Since we wanted to investigate the evolution of the emission lines in these late phases, we retain those as flare intervals. Also note that quiet interval Q7 has a relatively high count rate and shows significant low level variability in the light curve, but no obvious flares. We include it as a quiet interval after insuring that the Q7 spectrum shows no more than 1.2% variation compared to the summed quiet spectrum over all other intervals. Since Q7 represents almost

one-third of the quiet exposure time, including it increases the signal-to-noise of the summed quiet spectrum.

We used the IRAF package STSDAS (version 3.3.1, 2005 March 31) to split the timetag event lists into the quiet and flaring time intervals and then to extract spectra for these intervals. To split the event lists, we used the task 'inttag' (version 1.1, 2000 January 26). To extract the spectra, we used the task 'calstis' (version 2.18, 2005 February 15) with the best calibration reference files available on 2005 July 10. The calibration process removed radial velocity shifts caused by orbital motion of the spacecraft around the Earth and the Earth around the Sun. Hence, every extracted spectrum is in (the same) heliocentric reference frame. Table 2 provides the UT and Julian Date (JD) at the start of each exposure.

YZ CMi has a measured rotation velocity $v \sin i = 6.5 \text{ km sec}^{-1}$ (Delfosse et al. 1998). With a nominal radius of $0.2 R_{sun}$, this corresponds to a minimum period of 1.6 days, considerably longer than the total (consecutive) elapsed time of the HST exposures (~ 0.4 days). The individual exposures comprise $< 2\%$ of the minimum period, indicating negligible change in the location of a given active region during a single exposure. We do not see strong evidence for smooth (non-flaring) variability within a given orbit as was found by Robinson et al. (1999) in their near-ultraviolet photometric observations of YZ CMi using HST with the High Speed Photometer instrument. Our analysis of the STIS spectroscopic data is not presently suitable for comparison with their flare frequency analysis, but it would be interesting to reanalyze the MAMA timetag data in sum over shorter time intervals to more rigorously identify individual flares. However, this is beyond the scope of the present paper.

2.1. Light Curves and Spectra

Figure 1 and Table 1 show that YZ CMi was in an obvious flaring state for approximately 40% of the total 224 minutes of exposure time comprising the six separate exposures. The flux emitted in the near-ultraviolet bandpass sampled here (2300-3050Å) is approximately $4.2 \times 10^{-12} \text{ ergs sec}^{-1} \text{ cm}^{-2}$ during quiet periods. Using a distance of 6 parsecs for YZ CMi, the quiescent energy emitted from the visible hemisphere during the 224 minutes of exposure was $\sim 1.2 \times 10^{32}$ ergs, while the energy emitted by flares was $\sim 1 \times 10^{31}$ ergs, giving a total energy in this bandpass of $\sim 1.3 \times 10^{32}$ ergs. The flare energy comprises $\sim 8\%$ of the total.

Figure 2 illustrates the spectrum summed over all quiet intervals. The line identifications were made using the Chianti database (Dere et al. 1997, Landi et al. 2006). Clearly most of the emission lines in the near-UV come from Fe II, with the notable addition of the Mg II h and k lines and minor contributions from Si II, S II and Al II.

Figure 3 shows the summed spectrum over all flare intervals, with the quiet spectrum subtracted. Note that subtracting the quiet spectrum without scaling assumes that the area covered by the flare is negligible compared to the area of the visible hemisphere of the star. As discussed in Section 3, the flare area required to best match the observed Mg II k emission to the model predictions is $\sim 0.5\%$ of the observed surface, which supports the assumption that the flare area coverage is negligible. The flare-only emission shown in Figure 3 is primarily evident in the Mg II and Fe II lines, which are enhanced by a similar amount ($\sim 10\%$) over the quiet spectrum. Significant broadening in the Mg II lines is also apparent in this flare-only spectrum, and is discussed further in section 2.2 below.

Table 3 gives the energy breakdown between lines and continuum for the flare intervals individually and in sum. The first column shows the excess flare line flux calculated from the subtracted spectrum (flare interval - quiet), with the value in parentheses being the ratio of the flare line flux to the total (line + continuum) flux. The second column shows the same calculation for the continuum. Thus the values in parentheses represent the relative importance of lines and continuum to the excess flare emission, and sum to 1 in each case. As typically seen in stellar flares (e.g. Hawley & Pettersen 1991; Hawley et al. 2003) the larger flares are dominated by the continuum contribution, e.g. F2a, F4, F7 and F9a where $\sim 70\text{-}90\%$ of the energy is contained in the continuum. Two of the flares (F1 and F3), actually showed negligible line enhancements (formally negative but within the uncertainties of being small scale variability) but well-detected continuum enhancements. A large M dwarf flare was recently observed with GALEX with a broad bandpass NUV filter (Robinson et al. 2005), and analyzed assuming that all of the NUV emission was from the continuum. This appears to be reasonably justified by our analysis of the NUV flare spectra presented here. However, some smaller flares (F5, F8), and the decay phases of large flares (F2b, F2c, F9b), emit as much as 50% of their energy in the emission lines. In sum, the flaring intervals show that most flare energy is emitted in the continuum (77% compared to 23% in line emission), while the quiet spectrum is dominated by the emission lines, with 65% of the energy emitted in lines compared to 35% in the continuum.

The NUV emission line energy is quite evenly divided between Mg II and Fe II in this bandpass, with the Fe II/Mg II energy ratio being 0.97 in the quiet spectrum, and 1.01 in the flare spectrum. Each Mg II line carries much more energy than any individual Fe II line, but there are a large number (78) of identified Fe II lines in this region, which makes them energetically important in sum. Our results for the quiet ratio are in agreement with those found in Linsky et al. (1982).

2.2. Flares

The Mg II lines undergo significant changes in their line profiles during the flaring intervals. Figure 4 shows the Mg II k line profiles for the individual flares (F1-10), obtained from the summed spectra over the extent of each flaring episode. Flares F2 and F9 were large enough that it was possible to split them up into impulsive, peak and decay phases, shown as F2abc and F9abc in Figure 4. The quiet flare profile is shown for comparison as the dotted line in each panel. It is clear that the quiet flux dominates the total even during flares, indicating that the flare area coverage is very small, and that Mg II k is already a very strong line even in the quiet chromosphere. This behavior is similar to $H\alpha$, which also responds only slightly to flares in early-mid M dwarfs (e.g. Hawley et al. 2003), though it responds more strongly in late M dwarfs (cf. Liebert et al. 1999). This is in contrast to lines such as He I and II, and the higher order Balmer lines, which become significantly stronger during flares, often dwarfing the quiet contribution to the line flux (Hawley & Pettersen 1991).

Figure 5 shows the subtracted profiles for each flare (i.e. flare - quiet, as in Figure 3), in order to examine possible velocity shifts during the flare. The flares are shown on the same vertical scale such that strong flares have significant excess emission, and small flares have very little. It is clear that some flares (F1, F2, F3, F7, F10) show a blue wing enhancement and red wing deficit, while others show the opposite behavior (red wing enhancement and blue wing deficit - F4, F9) and still others show both blue and red enhancements (F5, F8) or deficits (F6). For simplicity, we use only the Mg II k line in the following analysis, as the Mg II h line exhibited very similar behavior in all cases.

The flares are grouped according to the appearance of the excess flare emission in Figure 6 (blue enhancements) and Figure 7 (red enhancements), with the left panels showing Mg II k and the right panels the strong Fe II UV1 line at 2600.2\AA . In general, the enhancements seen in Mg II k are also seen, albeit at a lower level and with poorer signal-to-noise ratio, in the Fe II data, as expected since these lines are formed in approximately the same temperature region of the atmosphere. Simple Gaussian fits to the enhancement features give wavelength shifts for each of these flares, as shown in Table 4. The shifts are not large, typically a few km/sec in both the upward (blue shift) and downward (red shift) directions. The Sun also shows such velocity shifts even outside of obvious flares. These have been attributed to asymmetric heating in active region loops (Winebarger et al. 2002).

To verify that these apparent velocity shifts are not artifacts of the data reduction, we compared the magnitude and sense of the shift in each flare with the peculiar velocities of HST and the Earth during the time period in the orbit that the flare occurred, and found no correlation. We see no evidence that the observed velocity shifts are instrumental in nature,

and therefore presume that they represent real effects in the NUV emission lines emitted by the star. We discuss the velocities compared to those expected from our flare models in Section 3 below.

Figure 8 shows the time evolution of the Mg II k emission for the largest flares, F2 and F9. Flare F2 exhibits rather simple behavior, with the narrow central profile strongly enhanced on the blue side in the impulsive phase (F2a), and decreasing monotonically during the flare decay (F2b, F2c). In contrast, flare F9 is quite unusual, initially (F9a) showing a strong red enhancement in the central profile, but then developing very broad, symmetric wings in F9b. Upon closer inspection of Figure 4, it appears that there is evidence for similarly broad wings in F7 and F9a. These data are reminiscent of those in Doyle and Byrne (1987) where extensive, symmetric line broadening was seen in the hydrogen Balmer lines during a flare on YZ CMi. Broad hydrogen lines during flares are usually interpreted as being due to Stark broadening (Donati-Falchi et al. 1985, Hawley and Pettersen 1991, Johns-Krull et al. 1997, Jevremovic et al. 1998) but Doyle and Byrne were unable to find a satisfactory fit to the data with Stark profiles. Instead they inferred symmetric red and blue shifted emitting regions, or turbulent motions, of order a few hundred km sec⁻¹. This is typical of the broad component often seen in transition region and coronal emission lines which is often ascribed to overlapping emission from multiple explosive microflaring events, leading to high velocity mass motions (Antonucci et al. 1993, Wood et al. 1996, Wood, Linsky & Ayres 1997, Vilhu et al. 1998). However, those broad components are not associated with large flares, but appear even in the quiescent spectra of active (earlier-type) stars, and the Sun. The phenomenon we have observed appears to be directly related to the large flare heating event F9, and does not appear in quiescence or in the other flaring events (except possibly flare F7). In particular it does not occur in the other large flare we observed, flare F2.

In the present case, we do not expect that Stark broadening will be important for the Mg II resonance lines. Fleurier, Sahal-Brechot & Chapelle (1977) determined experimentally that the Stark broadening of these lines varied with core width between 0.05-0.10Å, and wings extending to ~ 0.1-0.2Å, for temperatures of 1–3×10⁴K and an electron density of $N_e = 10^{17}$ cm⁻³, much higher than expected in the M dwarf atmosphere. Figure 9 illustrates a simple Gaussian fit to the underlying broad component in F9b yielding a redshift of $0.5\text{\AA} \pm 0.08\text{\AA}$ (53 ± 8 km sec⁻¹) and FWHM of $2.36\text{\AA} \pm 0.58\text{\AA}$ (250 ± 60 km sec⁻¹). If interpreted as velocities, the FWHM would suggest turbulent emitting material with typical speeds > 100 km sec⁻¹ within a bulk condensation moving downward at roughly 50 km sec⁻¹. Both the bulk and turbulent velocities exceed the sound speed in the chromosphere, which is roughly 10-20 km sec⁻¹. Adopting a chromospheric mass density of 1×10^{-10} g cm⁻³ during the flare (Allred et al. 2006) and a Mg II emitting region of height 300 km (see Figures 10 and 11

below) along with a flare area of 0.5% of the visible stellar surface, the kinetic energy implied by chromospheric material moving at such large velocities far exceeds the energy radiated by the flare, by several orders of magnitude.

Wood et al. (1996) found that the Mg II h and k lines in HR 1099, an active RS CVn binary system, showed a broad component during quiescence that looked similar to the broad components observed in the C IV transition region resonance lines, with FWHM $\sim 170 \text{ km sec}^{-1}$. They were skeptical, as we are, that the dense, optically thick chromosphere could respond to explosive microflaring events to drive mass motions at these velocities, and carried out detailed modelling that led them to suggest that opacity effects in the line wings might account for the observed broadening. Again however, these effects were associated with the star in quiescence, not in the midst of an obvious strong flare.

3. Comparison to Flare Models

Recently, Allred et al. (2005, 2006) produced models of solar and stellar flares aimed at understanding the chromospheric and transition region emission. The models use solutions to the 1-D equations of radiative hydrodynamics, including non-LTE radiative transfer in H, He and Ca II, with flare heating provided by an electron beam. The results include predictions of atmospheric structure (temperature, density profiles), velocity and line profiles at many time steps during an episode of flare heating. We used the results of their preflare and F10 models to investigate the Mg II k emission during the YZ CMi flares. The F10 model used here represents an average mid-flare atmosphere near a time step of $\sim 85 \text{ sec}$; see Allred et al. (2006). Note that the F10 model refers to electron beam heating of $10^{10} \text{ ergs sec}^{-1} \text{ cm}^{-2}$ during the model flare and is not to be confused with our observed F10 flare presented in Section 2 above.

Since the Allred et al. models do not predict Mg II emission line profiles, the preflare and F10 models were further analyzed with the ‘RH’ non-LTE radiative transfer code described in Uitenbroek (2001). The RH code is based on the Multi-level Accelerated Lambda (MALI) formalism of Rybicki & Hummer (1991, 1992), which allows both bound-bound and bound-free radiative transitions to overlap in wavelength. It also includes the effects of partial redistribution for strong bound-bound transitions such as Mg II h and k.

Figure 10 shows the temperature and density (electron, hydrogen) structure of the preflare atmosphere, together with the resulting Mg II k line profile and the contribution function. Figure 11 is a similar plot for the model F10 flaring atmosphere. The contribution function indicates the atmospheric height where the observed emission of interest is produced.

It is defined as the integrand in the equation for the emergent intensity:

$$I_\nu(0) = \frac{1}{\mu} \int_z S_\nu \chi_\nu e^{-\tau_\nu/\mu} dz \quad (1)$$

where $I_\nu(0)$ is the emergent intensity at frequency ν , μ is the cosine of the angle between the vertical and the emergent ray (we show the results for $\mu = 1$, i.e. a ray that emerges vertically), S_ν is the source function, χ_ν and τ_ν are the monochromatic opacity and optical depth respectively, and z is the atmospheric height.

As shown in the figures, the Mg II k line is formed in the upper chromosphere over a temperature range from 8000K (line wings) to 20,000K (line core). At 20,000K the density is lower, hence there is relatively less emitting material. This lower emission in the line core causes the central reversal in the line profile (see Figure 10). In the flaring atmosphere, there is an outward directed velocity where the core is formed, producing an asymmetric profile (see Figure 11) with a blue-shifted core. The contribution function (center panel of Figure 11) also indicates that the red wing is formed in a lower, denser region than the blue wing. Therefore, more flux is produced in the red wing.

We scaled the model flare line profile by 0.5%, subtracted it from the pre-flare line profile and smoothed it to the R=33,000 resolution of the data to produce the Mg II k subtracted (flare-quiet) model line profile shown in Figure 12. Note that at this resolution, the prominent central reversals in the model profiles are much reduced, although the models still do not have the smooth appearance of the observed line profiles in Figure 4. Nevertheless, the subtracted flare profile in Figure 12 looks quite similar to the observed profile during the impulsive phase of flare F9 (i.e. F9a, see Figure 8). The velocity shifts implied by the red-shifted emission are $\sim 4 \text{ km sec}^{-1}$ in the model profile, and $\sim 13.5 \text{ km sec}^{-1}$ in the observed profile.

However, the models do not reproduce the upward moving Mg II k material seen in the observed blue enhancement flares (Figure 6), nor do they show the very broad component in the decay phase of flare F9 (i.e. F9b, see Figure 9). In fact, if the broadening is interpreted as being due to emitting material moving with high velocity, the models never produce anything close to the velocities required at the depth of the Mg II emitting region.

Alternatively, the very broad wings seen in flare F9 may be due to enhanced redistribution of photons from the optically thick Doppler core to the less thick radiative damping wings, due to some process associated with the flare. Comparing quiet and flare profiles in Figure 4 suggests that the line core is saturated, even in the quiet atmosphere, so redistribution is likely to be important. The Allred et al. dynamical simulation includes the effects of the electron beam on atmospheric heating and the statistical equilibrium of H, but not Mg. The RH code that we use to generate spectra from the Allred et al. flare model includes a

standard implementation of partial redistribution. A “coherency fraction” (see Uitenbroek 2001, eqn. 13) mixes coherent scattering and complete redistribution in proportion to the depopulation rate (due to radiation and inelastic collisions) and elastic collision rate, respectively. Typically, elastic collisions are due to van der Waals and Stark broadening. However, the RH code does not include the contribution to the elastic collision rate due to interactions with the electron beam.

We speculate that the inclusion of the beam collisions would enhance the collisional rates, increasing the redistribution of line core photons into the wings and possibly producing the far wing line emission seen in the data. We plan to investigate this possibility in our next generation of flare models.

4. Summary

We analyzed six orbits of HST/STIS near-ultraviolet spectroscopic data on YZ CMi and found that the star was flaring approximately 40% of the time. The flares contributed $\sim 8\%$ of the energy observed in the near-ultraviolet (2300-3050Å) during the 224 total minutes of exposure time. Ten flaring and eight quiet intervals were identified, and two of the flares (F2, F9) were large enough to divide into sub-intervals to study the time evolution of the near-ultraviolet emission during those flares. The Mg II k emission line was examined in detail and found to change significantly between different flares, showing blue enhancements in some flares, red enhancements in others, and symmetric enhancements in the wings or core in still others. This indicates that Mg II emitting material may experience outward or inward directed velocities (i.e. evaporation or condensation) depending on the individual flare heating. The strongest Fe II line (UV1) showed similar behavior to the Mg II k line. Further, flare F9 showed a remarkable line broadening, which fit a Gaussian profile corresponding to a velocity FWHM of $\sim 250 \text{ km sec}^{-1}$. This velocity is highly supersonic, and if the broadening is interpreted as due to either symmetric mass motions, or turbulence, implies a kinetic energy during the flare that vastly exceeds the radiated energy (by several orders of magnitude). Overlapping emission due to explosive microflares, as has been suggested to explain the broad components observed in optically thin transition region emission lines, does not appear to be a physically plausible explanation for the emission from the Mg II lines which are formed in a dense, optically thick regime.

The data were compared to Mg II k line profiles generated using the preflare and F10 flare models of Allred et al. (2006) together with the RH code of Uitenbroek (2001). The model results indicate that the flare line profile has a red enhancement similar to that seen in the observed F9a spectrum, with velocity of a few km sec^{-1} . However, the models do not

predict the blue enhancements seen in some of the observed flares, nor does the Mg II emitting material attain velocities anywhere near those required to match the broad component of the Mg II k line seen in the F9b spectrum. The next step in the model calculations is to incorporate collisions with the electron beam into the Mg II k partial redistribution calculation, which may have the effect of increasing the emission in the radiative damping wings of the line, and could therefore explain the observed line broadening.

SLH, LMW and JCA acknowledge the support of STScI grants HST-AR-10312, HST-GO-10525, and NSF grant AST-0205875. The authors are grateful to Han Uitenbroek for allowing us to use his excellent RH code and helping with the implementation of the model atoms. Useful discussions were held with Rachel Osten, Phil Judge, Chris Johns-Krull, Andrew Becker and John Bochanski. We also thank the anonymous referee, whose substantive comments helped us to improve the paper.

REFERENCES

- Allred, J. C., Hawley, S. L., Abbett, W. P., & Carlsson, M. 2005, *ApJ*, 630, 573
- Allred, J. C., Hawley, S. L., Abbett, W. P., & Carlsson, M. 2006, *ApJ*, 644, 484
- Antonucci, E., Dodero, M. A., Martin, R., Peres, G., Reale, F., & Serio, S. 1993, *ApJ*, 413, 786
- Dere, K. P., Landi, E., Mason, H. E., Monsignori Fossi, B. C., & Young, P. R. 1997, *A&AS*, 125, 149
- Donati-Falchi, A., Falciani, R., & Smaldone, L. A. 1985, *A&A*, 152, 165
- Doyle, G. & Byrne, P.B. 1987, *Cool Stars, Stellar Systems and the Sun*, Proceedings of the Fifth Cambridge Workshop, Lecture Notes in Physics, Vol. 291, edited by J. L. Linsky and R. E. Stencel. Springer-Verlag, Berlin, p.173
- Eason, E. L. E., Giampapa, M. S., Radick, R. R., Worden, S. P., & Hege, E. K. 1992, *AJ*, 104, 1161
- Fleurier, C., Sahal-Brechot, S., & Chapelle, J. 1977, *J. Quant. Spec. Radiat. Transf.*, 17, 595
- Hawley, S. L. & Pettersen, B. R. 1991, *ApJ*, 378, 725
- Hawley, S. L., et al. 2003, *ApJ*, 597, 535
- Jackson, P. D., Kundu, M. R., & White, S. M. 1989, *A&A*, 210, 284

- Jevremovic, D., Houdebine, E. R., & Butler, C. J. 1998, ASP Conf. Ser. 154: Cool Stars, Stellar Systems, and the Sun, 154, 1500
- Johns-Krull, C. M., Hawley, S. L., Basri, G., & Valenti, J. A. 1997, ApJS, 112, 22
- Joy, A. H. & Humason, M. L. 1949, PASP, 61, 133
- Kahler, S., et al. 1982, ApJ, 252, 239
- Kimble, R. A., et al. 1998, ApJ, 492, L83
- Kunkel, W. 1967, AJ, 72, 810
- Landi, E., Del Zanna, G., Young, P. R., Dere, K. P., Mason, H. E., & Landini, M. 2006, ApJS, 162, 261
- Liebert, J., Kirkpatrick, J.D., Reid, I.N., Fisher, M.D. 1999, ApJ, 519, 345
- Mathioudakis, M. & Doyle, J. G. 1989, A&A, 224, 179
- Mitra-Kraev, U. et al. 2005, A&A, 431, 679
- Osten, R. A., Hawley, S. L., Allred, J. C., Johns-Krull, C. M., & Roark, C. 2005, ApJ, 621, 398
- Perryman, M. A. C., et al. 1997, A&A, 323, L49
- Robinson, R. D., Carpenter, K. G., & Percival, J. W. 1999, ApJ, 516, 916
- Robinson, R.D. et al. 2005, ApJ, 633, 447
- Rybicki, G. B., & Hummer, D. G. 1991, A&A, 245, 171
- Rybicki, G. B., & Hummer, D. G. 1992, A&A, 262, 209
- Uitenbroek, H. 2001, ApJ, 557, 389
- van den Oord, G. H. J., et al. 1996, A&A, 310, 908
- Vilhu, O., Muhli, P., Huovelin, J., Hakala, P., Rucinski, S. M., & Collier Cameron, A. 1998, AJ, 115, 1610
- Winebarger, A. R., Warren, H., van Ballegooijen, A., DeLuca, E. E., & Golub, L. 2002, ApJ, 567, L89
- Wood, B. E., Harper, G. M., Linsky, J. L., & Dempsey, R. C. 1996, ApJ, 458, 761

Wood, B. E., Linsky, J. L., & Ayres, T. R. 1997, ApJ, 478, 745

Worden, S. P., Schneeberger, T. J., Giampapa, M. S., Deluca, E. E., & Cram, L. E. 1984,
ApJ, 276, 270

Table 1. Flare and Quiet Time Intervals

Expo	t_{Beg}	t_{End}	Label	Rate	$\sigma(\text{Rate})$
1	0	22	Q1	14.4	6.7
	22	32	F1	30.0	15.8
2	0	5	F2a	62.0	70.9
	5	10	F2b	38.7	9.7
	10	15	F2c	17.9	5.1
	15	40	Q2	7.7	5.6
3	0	17	Q3	12.2	5.0
	17	40	F3	25.7	13.4
4	1	4.5	F4	30.1	31.1
	4.5	15.5	Q4	7.6	7.8
	15.5	19	F5	43.3	24.2
	19	27.5	Q5	7.0	7.7
	27.5	30	F6	34.9	6.1
	30	37	Q6	10.2	5.9
	37	39	F7	164	121
5	0	1.5	F8	44.2	3.8
	1.5	37	Q7	21.0	7.1
6	0	8	Q8	8.0	8.0
	8	11.5	F9a	55.2	34.1
	11.5	17	F9b	37.4	17.9
	17	25	F9c	8.4	4.4
	25	36	F10	26.9	7.2

Table 2. Table 2: STIS Exposure Start Times

Expo	UT Date	UT Time	JD
1	2000 Feb 05	17:36:15	2451580.23351
2	2000 Feb 05	18:56:14	2451580.28905
3	2000 Feb 05	20:32:51	2451580.35615
4	2000 Feb 05	22:09:29	2451580.42326
5	2000 Feb 05	23:46:06	2451580.49035
6	2000 Feb 06	01:22:43	2451580.55745

Table 3. Energy Budget in Lines and Continuum

Interval	Lines (ratio)	Continuum (ratio)
	$10^{-13} \text{ ergs s}^{-1} \text{ cm}^{-2}$	
F1	-0.45 (-0.09)	5.50 (1.09)
F2a	1.71 (0.10)	14.85 (0.90)
F2b	4.12 (0.45)	4.98 (0.55)
F2c	0.42 (0.46)	0.49 (0.54)
F3	-0.32 (-0.17)	2.20 (1.17)
F4	1.15 (0.09)	12.36 (0.91)
F5	5.19 (0.41)	7.57 (0.59)
F6	1.56 (0.15)	9.11 (0.85)
F7	10.66 (0.22)	38.24 (0.78)
F8	4.52 (0.56)	3.61 (0.44)
F9a	5.94 (0.33)	11.84 (0.67)
F9b	5.22 (0.51)	4.97 (0.49)
F10	1.75 (0.30)	4.02 (0.70)
Total F	1.78 (0.23)	6.10 (0.77)
Quiescent	27.14 (0.65)	14.35 (0.35)

Table 1. Narrow Component Flare Velocity Shifts

Flare	λ_c Å	$\Delta\lambda_c$ Å	V (km/s)	ΔV (km/s)
F1	2803.53	0.02	−4.65	2.14
F2a	2803.53	0.04	−4.65	3.21
F3	2803.54	0.05	−3.58	5.35
F4	2803.70	0.03	13.52	3.21
F7	2803.56	0.04	−1.44	4.28
F9a	2803.70	0.04	13.52	4.28
F10	2803.59	0.04	1.59	4.28

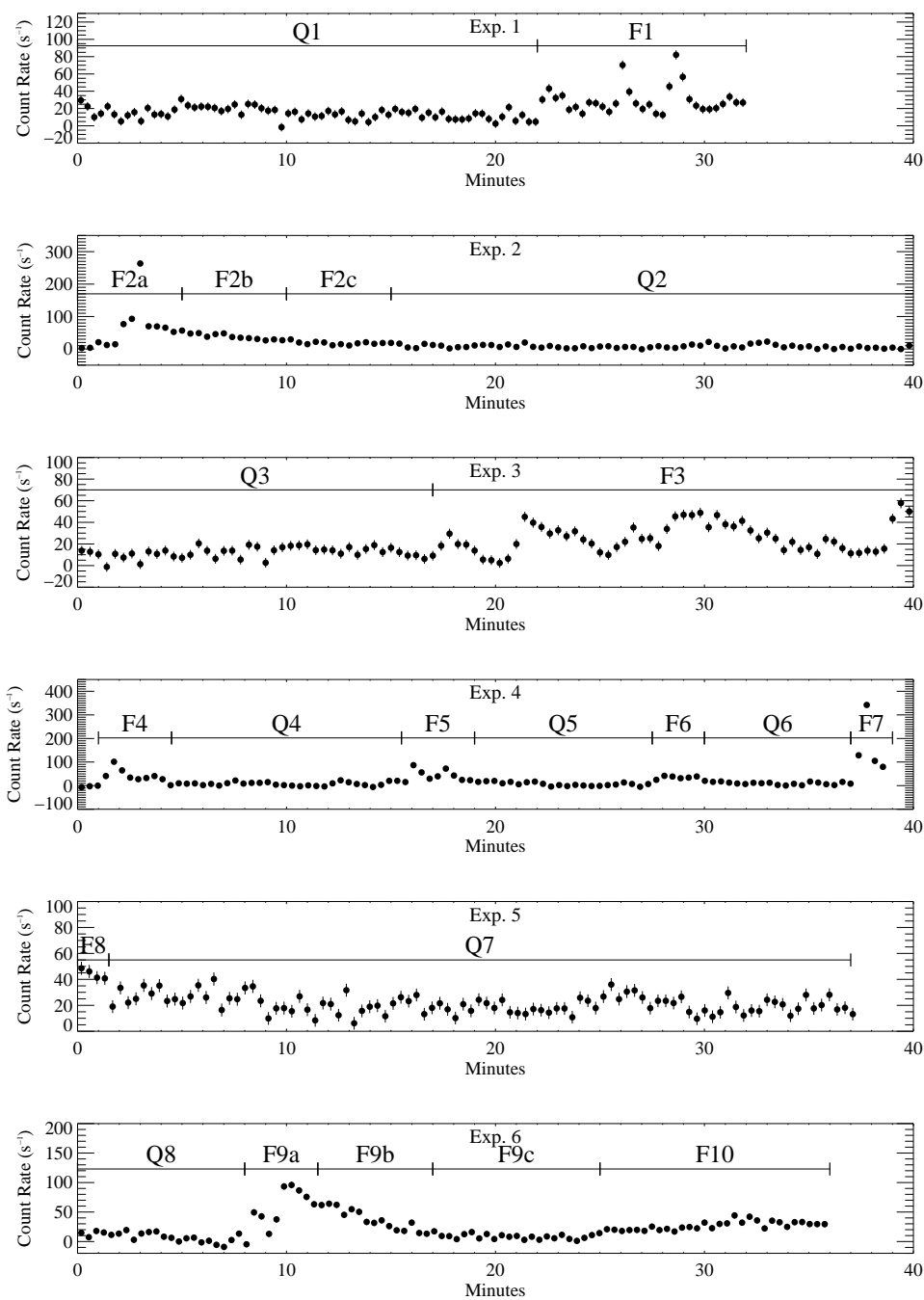


Fig. 1.— Light curves showing the total count rate integrated over the 2300-3050Å STIS E230M bandpass during each of the six exposures on YZ CMi. See text for details about the construction of the light curves. The flaring (F1-F10) and quiet (Q1-Q8) intervals are indicated.

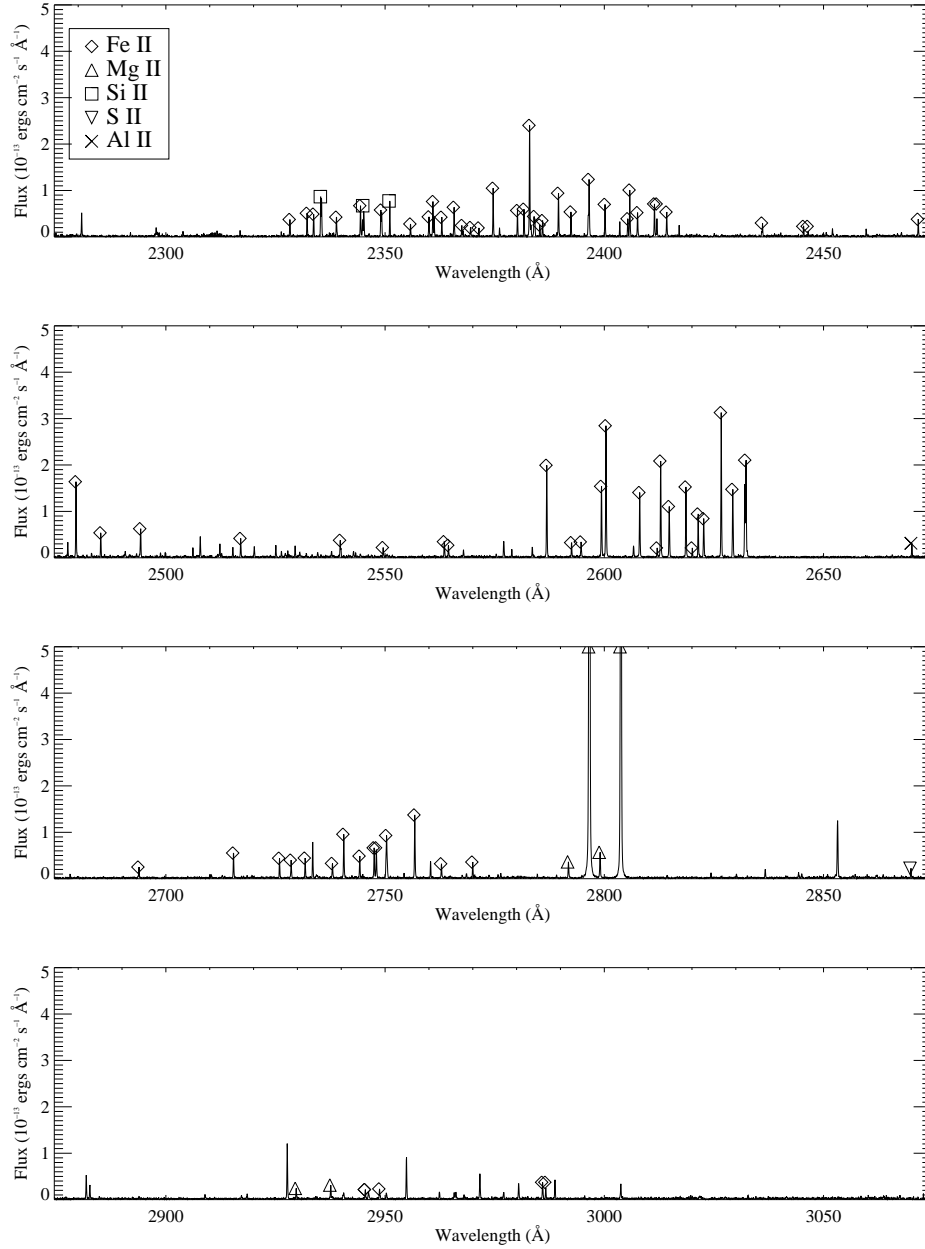


Fig. 2.— All of the quiet intervals from Figure 1 have been coadded to produce a high signal-to-noise quiet spectrum of YZ CMi in the near-ultraviolet. Emission lines identified in the Chianti database are labeled. The Mg II h and k lines extend off the figure, with peaks at 2.3×10^{-12} and 1.8×10^{-12} ergs sec⁻¹ cm⁻² respectively.

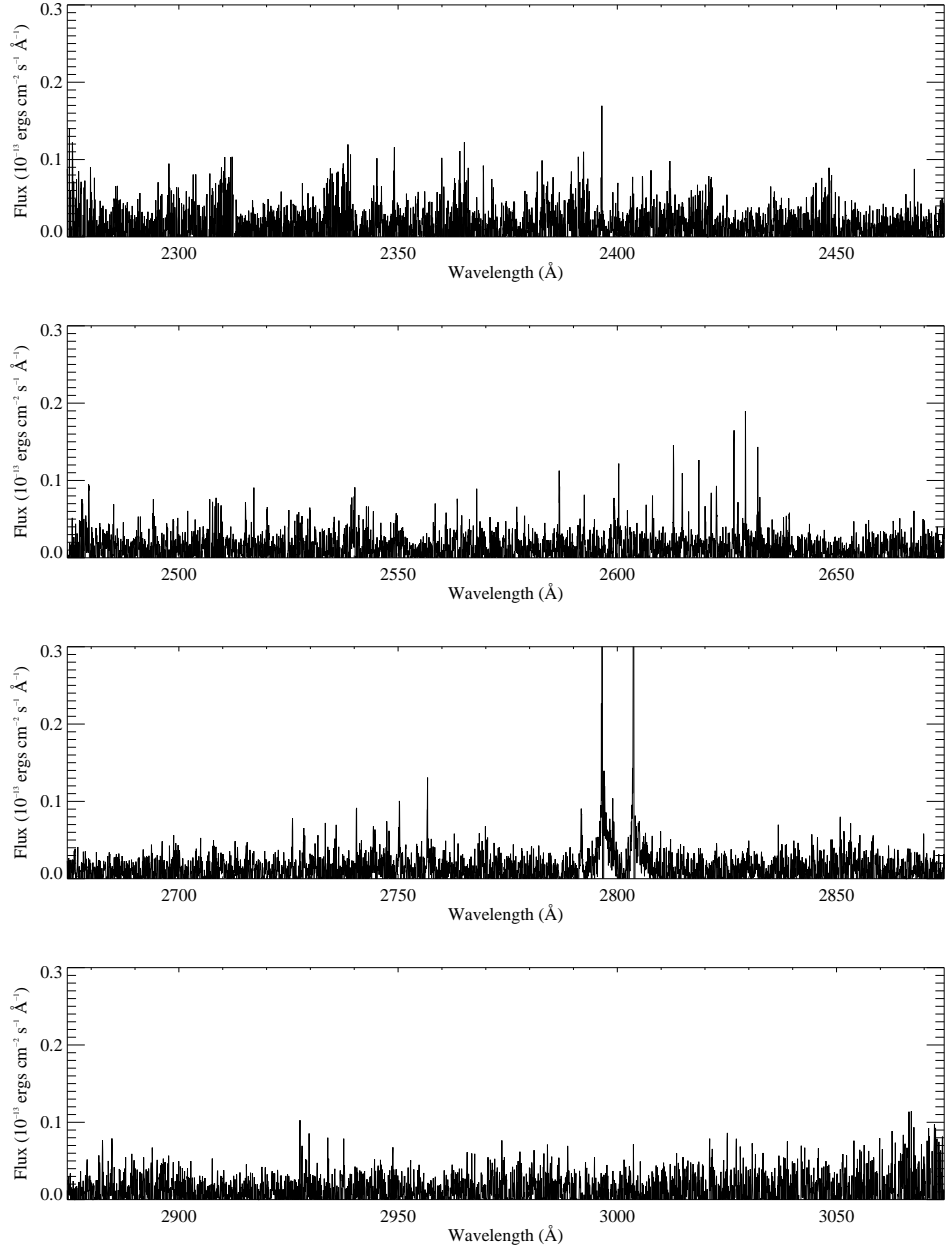


Fig. 3.— The flare intervals from Figure 1 were coadded to produce a flare spectrum, and the quiet spectrum from Figure 2 was subtracted to produce this flare only spectrum. The Mg II h and k lines extend off the figure, with peaks at 6.1×10^{-14} and 6.4×10^{-14} ergs sec^{-1} cm^{-2} respectively.

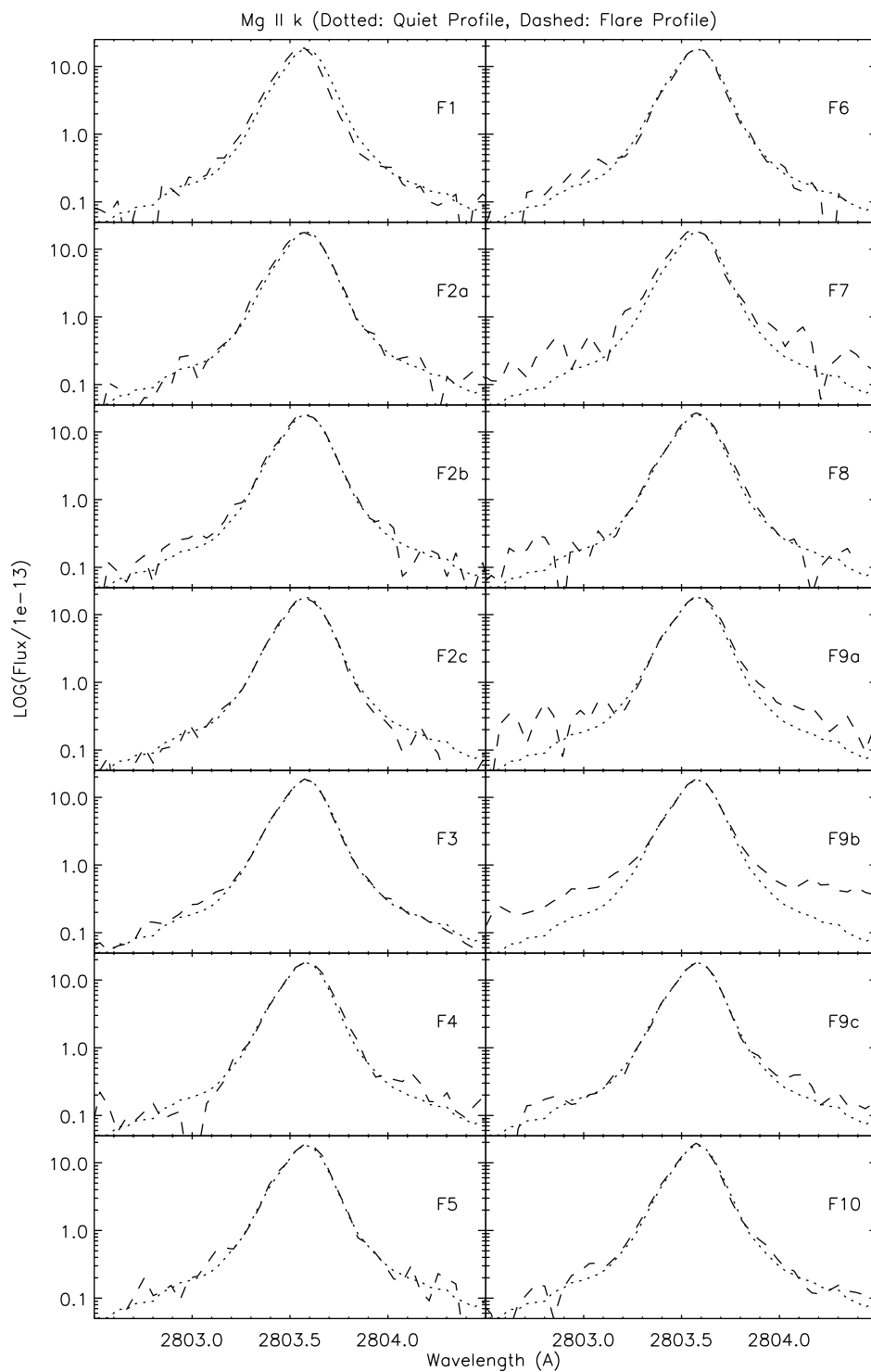


Fig. 4.— The Mg II k line profiles are shown for each of the flare intervals, including the three subdivisions of flares F2 and F9. The data are displayed on a log flux scale, so that enhancements in the line wings during the flares are evident. The quiet profile is included for comparison in each panel.

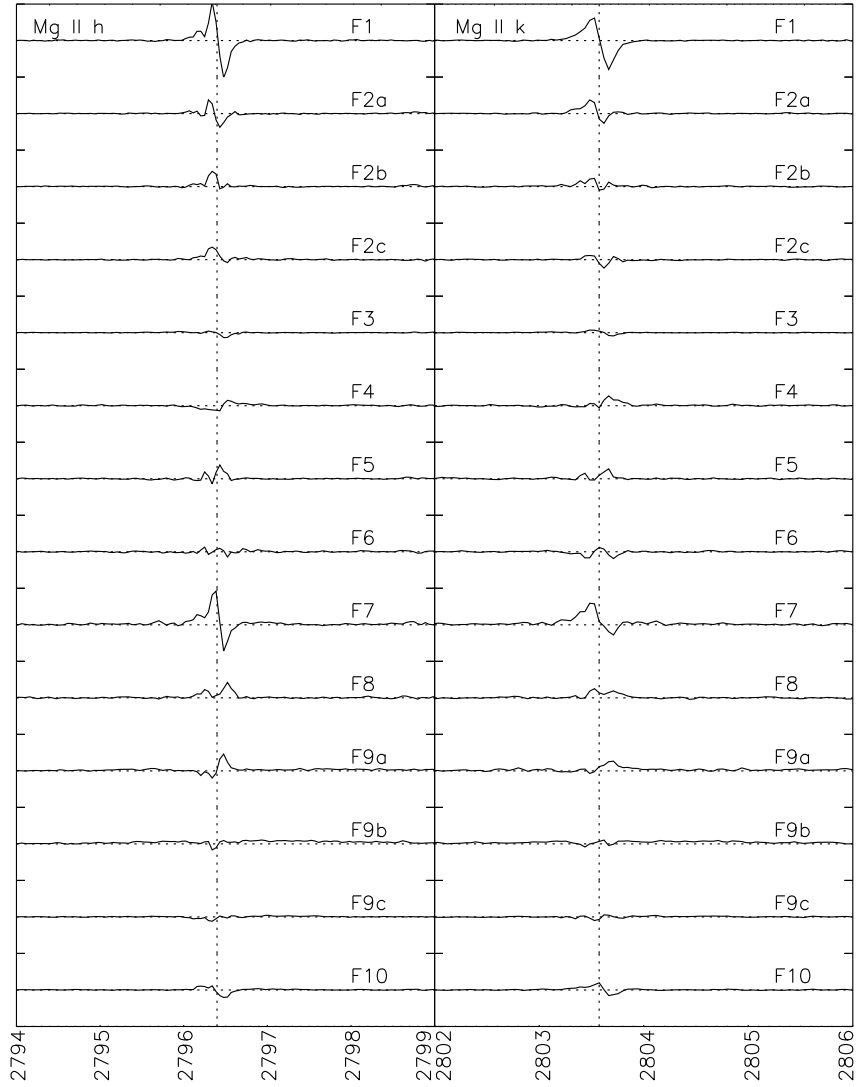


Fig. 5.— The subtracted (flare-quiet) line profiles are shown for Mg II h and k, indicating that the two lines behave very similarly. Each panel has the same scaling, so the relative amount of flare emission during each flare interval can be directly compared. The impulsive flares in F1 and F7 and the large F2 flare show the strongest response in the Mg II lines.

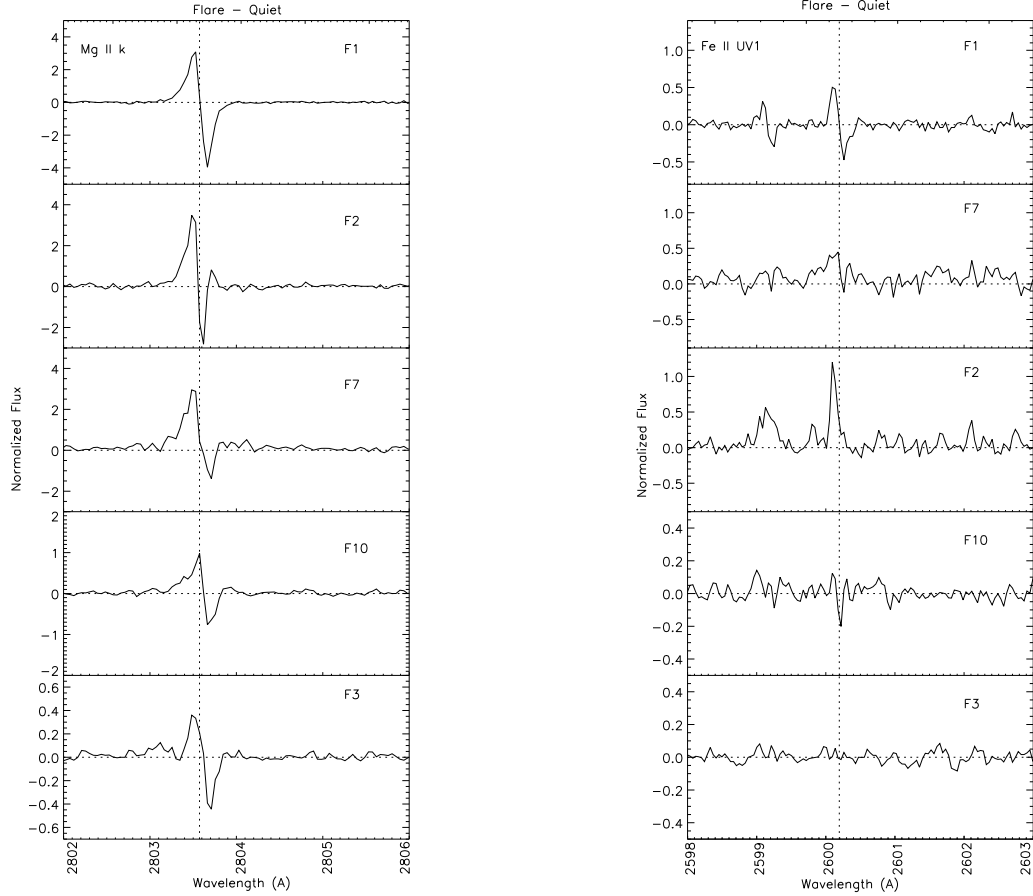


Fig. 6.— The subtracted (flare-quiet) line profiles for the Mg II k lines from Figure 5 that showed blue enhancements are illustrated in the left panels, in order from strongest to weakest emission enhancement. The Fe II UV1 line profiles for the same flare intervals are given in the right panels. Though noisier, the Fe II data generally show the same blue enhancements as the Mg II data.

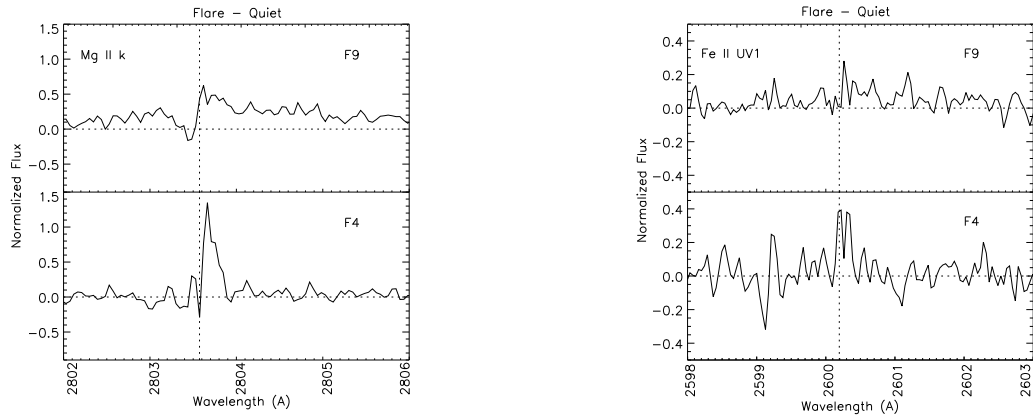


Fig. 7.— Same as Figure 6, but for the flares that showed red enhancements in Mg II k.

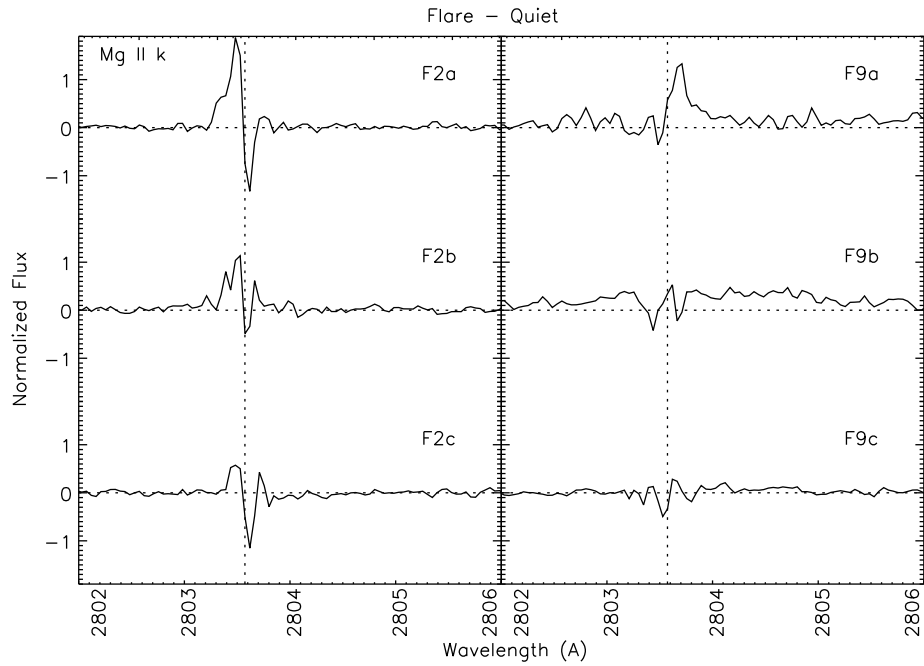


Fig. 8.— The time evolution of the Mg II k subtracted (flare-quiet) line profiles is illustrated for intervals F2abc and F9abc. Flare F2 shows consistent behavior throughout the impulsive and decay phases, while flare F9 changes from a narrow, red enhanced line in F9a to a symmetric but very broad line in F9b. See text and Figure 9 for further discussion of the broad line wings in F9b.

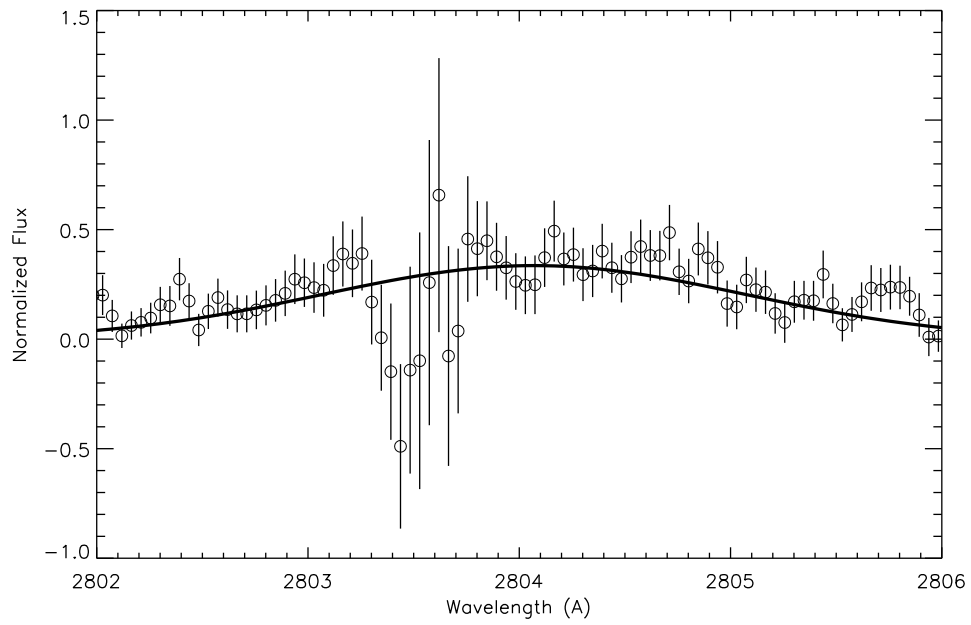


Fig. 9.— The Gaussian fit to the broad component of flare interval F9b is shown, together with the individual data points and uncertainties. The broad component is easily detected at the signal-to-noise ratio of these data. The fit parameters (given in the text) imply a FWHM of 250 km/sec for this emission component.

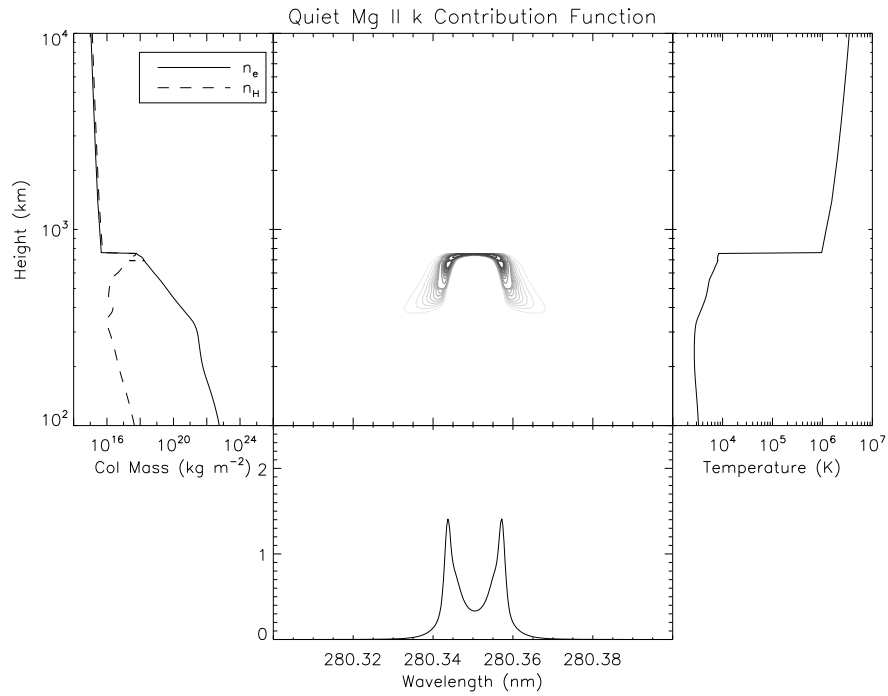


Fig. 10.— The model temperature and density distributions (right and left upper panels respectively), the Mg II k contribution function showing where the Mg II k emission is being produced (middle upper panel), and the resulting Mg II k line profile (bottom panel) are illustrated for the preflare (quiet) M dwarf model.

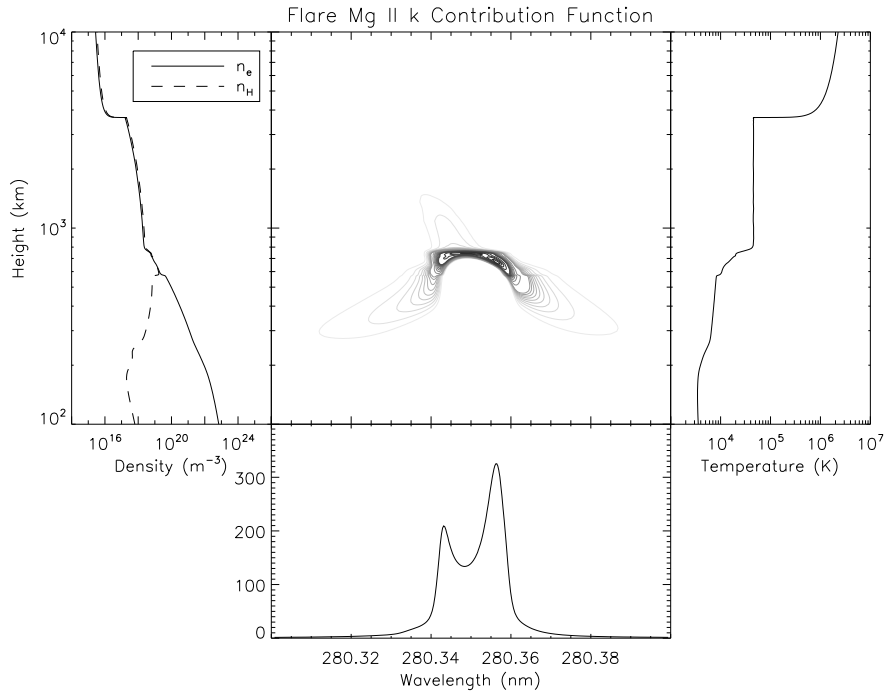


Fig. 11.— Same as Figure 10 for the flare F10 model. The flare model clearly shows the effect of beam heating on the chromospheric temperature and density distributions, and the contribution function indicates that the Mg II emitting region is asymmetric due to the velocity fields in the atmosphere. The line profile reflects this asymmetry.

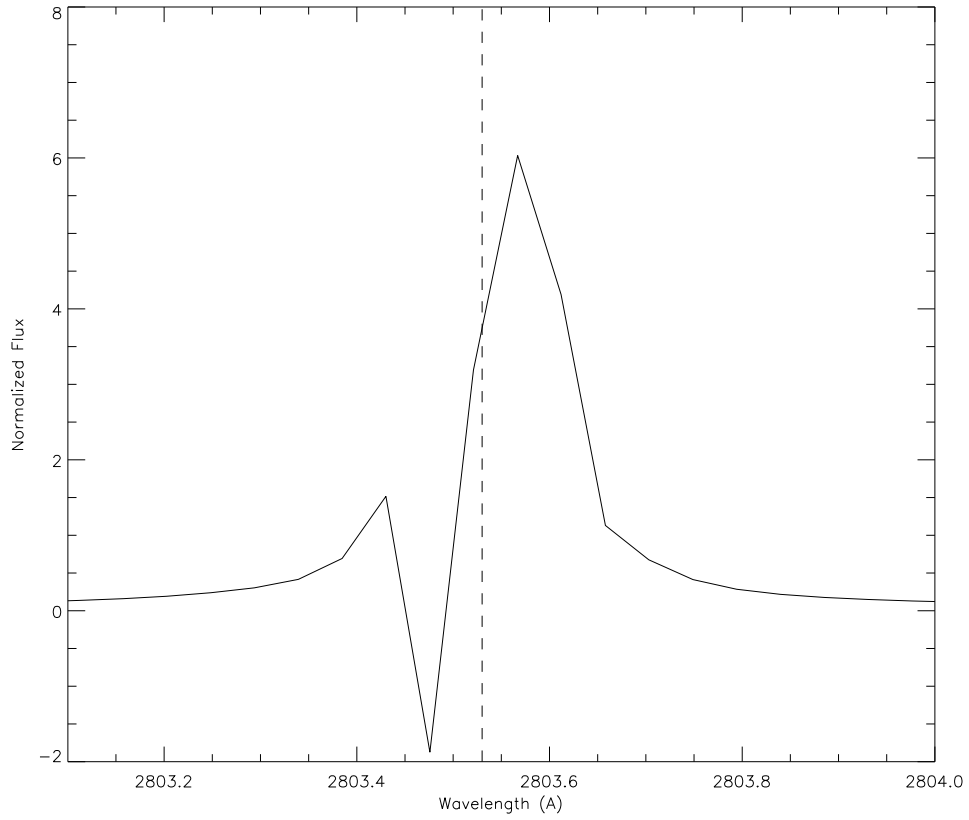


Fig. 12.— The Mg II k subtracted ($0.005 \times$ model flare - model quiet) line profile shows a red enhancement similar to that observed during flare F9a. The flare area coverage was adjusted so that the model flare emission is similar to the observed profile, giving a value for the flare area of 0.5% of the visible stellar surface.